Geophysical Journal International

Geophys. J. Int. (2010) **183,** 1348–1361 doi: 10.1111/j.1365-246X.2010.04790.x

Geophysical muon imaging: feasibility and limits

N. Lesparre,[1] D. Gibert,[1] J. Marteau,[2] Y. Déclais,[2] D. Carbone[3] and E. Galichet[4]

[1] *Institut de Physique du Globe de Paris (UMR CNRS 7154), Sorbonne Paris Cité, Paris, France. E-mail: gibert@univ-rennes1.fr*
[2] *Institut de Physique Nucléaire de Lyon (UMR CNRS 5822), Lyon, France*
[3] *Istituto Nazionale di Geofisica e Vulcanologia – Sezione di Catania, Catania, Italy*
[4] *Conservatoire National des Arts et Métiers, Paris, France*

Accepted 2010 August 20. Received 2010 August 20; in original form 2010 April 20

SUMMARY

We study the possibility of muon radiography as a tool to investigate space and time changes in the internal density distribution inside geological structures. Previous work has shown the practical applicability of this method. Nevertheless, quantitative information on factors which impose limitations on it are still sorely lacking in the literature. We discuss the main issues that can influence the final result of a geophysical imaging experiment. In particular, with the view of optimizing the signal-to-noise ratio, we address issues concerning (i) the energy spectrum for muons arriving at different zenith angles, (ii) the muon propagation model through matter and (iii) the characteristics of the muon detector (telescope) that we have designed to perform experiments of muon radiography against the harsh environment usually encountered in the active zone of a volcano. We thus identify factors that can induce either static or dynamic effects and that should be taken into account. We also define a feasibility eq. (32) relating the geometrical characteristics of the telescope and the duration of the experiment to the expected density resolution, in turn a function of the geometrical characteristics of the target structure. This relation is especially important to define the applicability domain of muon radiography and it is utilized to test the suitability of the method to investigate the density distribution inside some candidate target structures.

Key words: Inverse theory; Spatial analysis; Tomography.

1 INTRODUCTION

The interest in using muon imaging for Earth Sciences purposes soon arose after the discovery of cosmic rays (Auger 1941; Leprince-Ringuet 1945; Gaisser 1990; Crozon 2005) and muons (Neddermeyer & Anderson 1937, 1938), when it was realised that muons of cosmic origin are able to cross hundred of meters and even kilometres, of rock with an attenuation mainly related to the amount of matter encountered along their trajectory (Nagamine 2003). The very first studies relevant to muon imaging were motivated by the need to characterise the geological burden overlying underground laboratories hosting particles detectors (George 1955). Later, interest for applications other than those directly related to underground laboratories emerged when lighter and mobile detectors became available for field experiments. Early examples are the archaeological investigations performed in the Egyptian Chephren pyramid by Alvarez *et al.* (1970) and the theoretical study of Malmqvist *et al.* (1979), concerning the utility of muon imaging in mining geophysics.

More recently, the interest for muon imaging has been renewed, following significant improvements in particle detectors and miniaturised electronics, which allowed experiments in out-of-the-lab conditions. In particular, a Japanese team demonstrated the feasibility of the method to detect both spatial and temporal changes of density inside volcanoes (Nagamine 1995; Nagamine *et al.* 1995; Tanaka *et al.* 2001, 2003, 2005, 2007a,b,c, 2008, 2009a,b; Tanaka & Yokoyama 2008).

Muon imaging relies on the well-known radiography concept and the attenuation of the flux of muons crossing the body of interest is used to derive the amount of matter encountered along the muon trajectories. Depending on both its density and size, the target object will interact more or less with the flux of muons crossing it. In this paper, we define the opacity, ϱ, as (see Table 1 for a definition of symbols):

$$\varrho(L) \equiv \int_L \rho(\xi)\,\mathrm{d}\xi, \tag{1}$$

where ϱ is expressed in $\mathrm{g\,cm^{-2}}$, ρ is the density and ξ is the coordinate measured along the trajectory L of the muon crossing the volume of rock.

The attenuation, from which the opacity ϱ is deduced, is determined by comparing the flux, Φ, measured after crossing the geological target to the incident flux, Φ_0, measured in open sky condition. Obviously, a very precise estimate of Φ_0 is of a critical importance for it directly influences the determination of the attenuation of the flux produced by the geological body. Some Φ_0 models, proposed by different authors, are discussed in Section 2, but, due to their yet strong uncertainty, the experimental flux measured in

Table 1. Meaning and physical unit of the principal symbols used in the present study.

Symbol	Unit	Meaning
L	m	length of ray path
D	m	distance between matrices of telescope
d	m	size of matrix pixels
ΔT	s	duration of measurement period
θ	rad or degrees	zenith angle
θ^*	rad or degrees	zenith angle corrected for Earth's sphericity
Ω	sr	total angular coverage of telescope
$\delta\Omega$	sr	angular resolution of a telescope
$N_x\, N_y$	$\in \mathbb{N}$	size of telescope matrix
$\mathcal{T}$	cm^2 sr	telescope acceptance
ρ	$\mathrm{g\,cm}^{-3}$	density
ϱ	$\mathrm{g\,cm}^{-2}$	opacity of rock layer (eq. 1)
$1-\alpha$		probability level of confidence interval
N	$\in \mathbb{N}$	number muons detected
ΔN	$\in \mathbb{N}$	discrepancy between the number muons detected for two different rock volumes
δN	$\in \mathbb{N}$	half-width of confidence interval of N
p	$\mathrm{GeV}\,c^{-1}$	momentum
E_0	GeV	energy of muon at sea level
$\hat{E}_0$	GeV	energy of muon on top of atmosphere
ΔE_0	GeV	energy loss of muon across the atmosphere
$E_{\min}$	GeV	minimum muon energy to cross a given opacity
Φ	$\mathrm{cm}^{-2}\,\mathrm{sr}^{-1}\,\mathrm{s}^{-1}\,\mathrm{GeV}^{-1}$	differential flux of muons
γ	$\in \mathbb{R}$	power-law exponent of differential spectrum
A		scale factor (i.e. amplitude) of differential spectrum
I	$\mathrm{cm}^{-2}\,\mathrm{sr}^{-1}\,\mathrm{s}^{-1}$	integrated flux

open sky condition for each experiment should instead be used to derive the attenuation.

Muon imaging generally deals with weak signals (i.e. low fluxes), with a low signal-to-noise ratio, which implies large errors bars on opacity and hence on density. As discussed in more details below, if the time sequence of muons arrivals follows a Poisson distribution, a given signal-to-noise ratio is reached when a given number of muons are detected. Consequently, the measurement period must be longer then a given threshold, to resolve a given density contrast. This constrain also limits the time resolution at which geophysical phenomena can be observed. In practice, this could lead to a situation of infeasibility for temporal imaging, if the characteristic time constant of the studied phenomena is shorter than the needed measurement duration.

Section 2 presents some models for the Φ_0 flux and the influence of static or dynamic effects on the flux are addressed. Section 3 briefly summarizes the rules governing the attenuation of muons by rocks and simple formulas are derived to quickly compute the attenuation and the flux Φ as a function of rock thickness (eqs 19-17). Section 4 presents an example of field telescope, together with its detection characteristics. The latter are used in the feasibility eq. (32), derived in Section 5. Finally, in Section 6, we use eq. (32) to determine the feasibility domain of the method, under different geological conditions.

2 SPECTRUM OF INCIDENT COSMIC MUONS Φ_0

2.1 The muon spectrum

Excepted in very particular situations where artificial sources of muons could be used to perform imaging of geological objects (see Nagamine 2003, for a discussion about such a possibility), all experiments performed to date used muons of cosmic origin, belonging to the so-called secondary cosmic rays. The latter are produced high in the atmosphere (typically 15 km) through interactions between primary cosmic rays, coming from outer space (mainly protons—82.4 per cent—and α particles—11.5 per cent when normalized in number of nucleons per GeV per nucleon, see Table 1.1 in Gaisser 1990) and atmospheric molecules (Gaisser 1990; Crozon 2005). When measured at the sea level, charged cosmic rays are mainly (63 per cent) composed of muons with a mean energy $\langle E_0 \rangle \approx 4$ GeV near the zenith (Gaisser 1990). However, the muon spectrum at sea level has a complex form, due to the competition between the interaction and decay of pions and kaons parents and the power-law behaviour inherited from the spectrum of primary cosmic rays and observed for energy $E_0 > 2$ TeV.

The flux of incident cosmic muons is of critical importance for geophysical imaging since it is used to determine the attenuation produced by the geological target. Consequently, any bias in the incident flux of muons will be converted into a bias in the density distribution inside the target. As will be seen in Section 3, muons with energy as low as several tens of GeV are able to cross several tens of meters of rock, making necessary to know the low-energy part of the muon spectrum. A huge amount of data is available to determine the surface flux of muons for energies up to 1 TeV and for different zenith angles $0 \leq \theta \leq \pi/2$. Despite the large data set available, significant discrepancies still exist among models recently published by several authors and we present some of them to give the reader a reasonable uncertainty concerning the muon source. These models are useful to simulate and design field experiments by either computing synthetic radiographies or estimating the duration of an experiment through the feasibility formula (32) discussed below. However, given the large number of published models, our review cannot be exhaustive and we invite the interested reader to refer to the paper of Gaisser & Stanev T. (2008) and to the data available on the web site of the Particle Data Group (http://pdg.lbl.gov).

There are two ways to derive the differential flux of muons $\Phi_0 \equiv \mathrm{d}N(E_0, \theta)/\mathrm{d}E_0$ (given in $\mathrm{cm}^{-2}\,\mathrm{sr}^{-1}\,\mathrm{s}^{-1}\,\mathrm{GeV}^{-1}$). The first approach consists in performing a full Monte Carlo simulation,

Table 2. Values of the parameters of model (2) determined by several authors.

Model	A_G	B_G	γ	$E^{cr}_{0,\pi}$ (0)	$E^{cr}_{0,K}$ (0)	r_c	E_0 range (GeV)	Reference
MS1	0.1258	0.0588	2.65	100	650	0	$100 - 10^5$	Volkova *et al.* (1979)
MS2	0.14	0.054	2.70	115/1.1	850/1.1	0	$100 - 10^5$ and $\theta < 70^\circ$	Gaisser (1990)
MS3	0.175	0.037	2.72	103	810	0	$300 - 2.5 \times 10^5$	Klimushin *et al.* (2001)
MS4	0.2576	0.054	2.77	115/1.1	850/1.1	0	2×10^3 -4×10^4	Aglietta *et al.* (1999)
MS5	0.26 ± 0.01	0.054	2.78 ± 0.01	115/1.1	850/1.1	0	500 -2×10^4	Ambrioso *et al.* (1997)

through which a large number of air showers, induced by primary nuclei, are generated. The computed muon production is then propagated and attenuated through the atmosphere, to obtain the flux at a given altitude. These computations can be accomplished through simulation codes like CORSIKA (Heck *et al.* 1998), which also allow to take into account the geomagnetic and altitude dependence. A second class of flux models is obtained by fitting more or less complicated empirical parametric curves to muon flux data measured at the sea level. The choice of a particular parametrization of the fitting curves may either be inspired by the physics involved in the production of muons from their parents (e.g. Gaisser 1990; Bugaev *et al.* 1998) or be guessed to provide a tight fit, regardless of the physical meaning of the parameters.

Some models of the above second class only consider the production of muons from the two-body decays of pions and kaons and assume a primary proton flux of the form $P_0 E_p^{-\gamma}$, with $P_0 \approx 1.8\,\mathrm{cm^{-2}\,sr^{-1}\,s^{-1}\,GeV^{\gamma-1}}$ and $\gamma \approx 2.7$. This approach yields the analytical form of the muon spectrum initially proposed by (Bugaev *et al.* 1970) and popularised by Gaisser (1990), which reads:

$$\Phi_G(E_0, \theta) = A_G E_0^{-\gamma} \left(\frac{1}{1 + \hat{E}_0 \cos\theta / E^{cr}_{0,\pi}} + \frac{B_G}{1 + \hat{E}_0 \cos\theta / E^{cr}_{0,K}} + r_c \right), \quad (2)$$

where the adjustable parameters are the scale factor A_G, the power index γ, the balance factor B_G, which depends on the ratio of muons produced by the kaons and the pions and the ratio r_c of the prompt muons to pions.

$\hat{E}_0$ represents the energy of muons on top of the atmosphere. The energies $E^{cr}_{0,\pi}$ and $E^{cr}_{0,K}$ may be interpreted as critical energies of pions and kaons for the vertical incidence (i.e. $\theta = 0$). These physical quantities should be non-adjustable parameters and should be determined through quantum mechanical calculus. However, most authors consider $E_{0,\pi}$ and $E_{0,K}$ as adjustable parameters when fitting model (2) to data sets. Table 2 recalls the best estimates of these parameters published by several authors.

The θ dependence in eq. (2) accounts for the larger thickness of the atmospheric layer crossed by the muons when the zenith angle increases. However, for large angles $\theta > 70^\circ$, a modified version θ^* is often used in (2) to account for the spherical geometry of the Earth. In fact, the curvature of Earth significantly reduces the thickness of atmospheric layer to be crossed by muons. We have,

$$\cos\theta^* = \sqrt{1 - \frac{1 - \cos^2\theta}{(1 + H_{atm}/R_{Earth})^2}}, \quad (3)$$

where $R_{Earth} = 6370$ km is the Earth radius and $H_{atm} = 32$ km is the altitude of production for muons with a trajectory at large angles.

The empirical spectrum model given by eq. (2) strongly overestimates the incident flux for $E_0 < 100/\cos\theta$ GeV and Tang *et al.* (2006) proposed a modified version of the original Gaisser's model. A version of this modified spectrum is used in the MUSIC Monte Carlo simulation code (Kudryavtsev 2009) with $r_c = 10^{-4}$ and

$$\hat{E}_0 = E_0 + \Delta E_0, \quad (4)$$

$$A_T = A_G \left(\frac{120 \cos\theta^*}{1030} \right)^{\frac{1.04}{(E_0 + \Delta E_0/2)\cos\theta^*}}, \quad (5)$$

where

$$\Delta E_0 = 0.00206 \left(\frac{1030}{\cos\theta^*} - 120 \right). \quad (6)$$

Table 3. Parameters of the fitting formula (7) for the vertical energy spectrum of conventional muons at sea level (data taken from Bugaev *et al.* 1998).

p range (GeV) GeVc^{-1}	A_B (cm^2 sr s GeV)$^{-1}$	α_0	α_1	α_2	α_3
$1 - 930$	2.950×10^{-3}	0.3061	1.2743	−0.263	0.0252
$930 - 1590$	1.781×10^{-2}	1.791	0.304		
$1590 - 4.2 \times 10^5$	1.435×10^1	3.672			
$> 4.2 \times 10^5$	10^3	4			

Other empirical models departing from the Gaisser's formula (2) and accounting for the low-energy range of the spectrum have been proposed by several authors. For instance, Bugaev *et al.* (1998) derived the following model equation:

$$\Phi_B(p) = A_B p^{-(\alpha_3 y^3 + \alpha_2 y^2 + \alpha_1 y + \alpha_0)}, \quad (7)$$

with $y \equiv \log_{10} p$ and where the momentum p verifies

$$p^2 c^2 = E_0^2 - E_\mu^2 \quad (8)$$

with $E_\mu = 0.10566$ GeV. When the momentum is expressed in GeV/c, as is usually the case in the particle physics literature, $c = 1$ in the formula above. Table 3 recalls both the numerical values of the α's and the E_0 ranges, derived by Bugaev *et al.* (1998).

The class of empirical spectrum models of Bugaev *et al.* (1998) is valid for a wide range of energy and was used as a reference by Hebbeker & Timmermans (2002), who fitted it to experimental data sets and found new normalisations for each set, through an iterative procedure. They obtained a new flux shape, independent of the starting Bugaev *et al.* flux and described by

$$\Phi_H(p) = A_H 10^{H(y)}, \quad (9)$$

where the function

$$H(y) = h_1 \frac{y^3 - 5y^2 + 6y}{2} + h_2 \frac{-2y^3 + 9y^2 - 10y + 3}{3} + h_3 \frac{y^3 - 3y^2 + 2y}{6} + s_2 \frac{y^3 - 6y^2 + 11y - 6}{3}, \quad (10)$$

with $h_1 = 0.144$, $h_2 = -2.51$, $h_3 = -5.76$ and $s_2 = 2.22$.

A major limitation of the models proposed by Bugaev *et al.* (1998) and by Hebbeker & Timmermans (2002) is that they account only for the vertical incidence, $\theta = 0$. To overcome this limitation, the empirical parametrization proposed by Reyna (2006) can be utilised, which allows to calculate the differential muon intensity

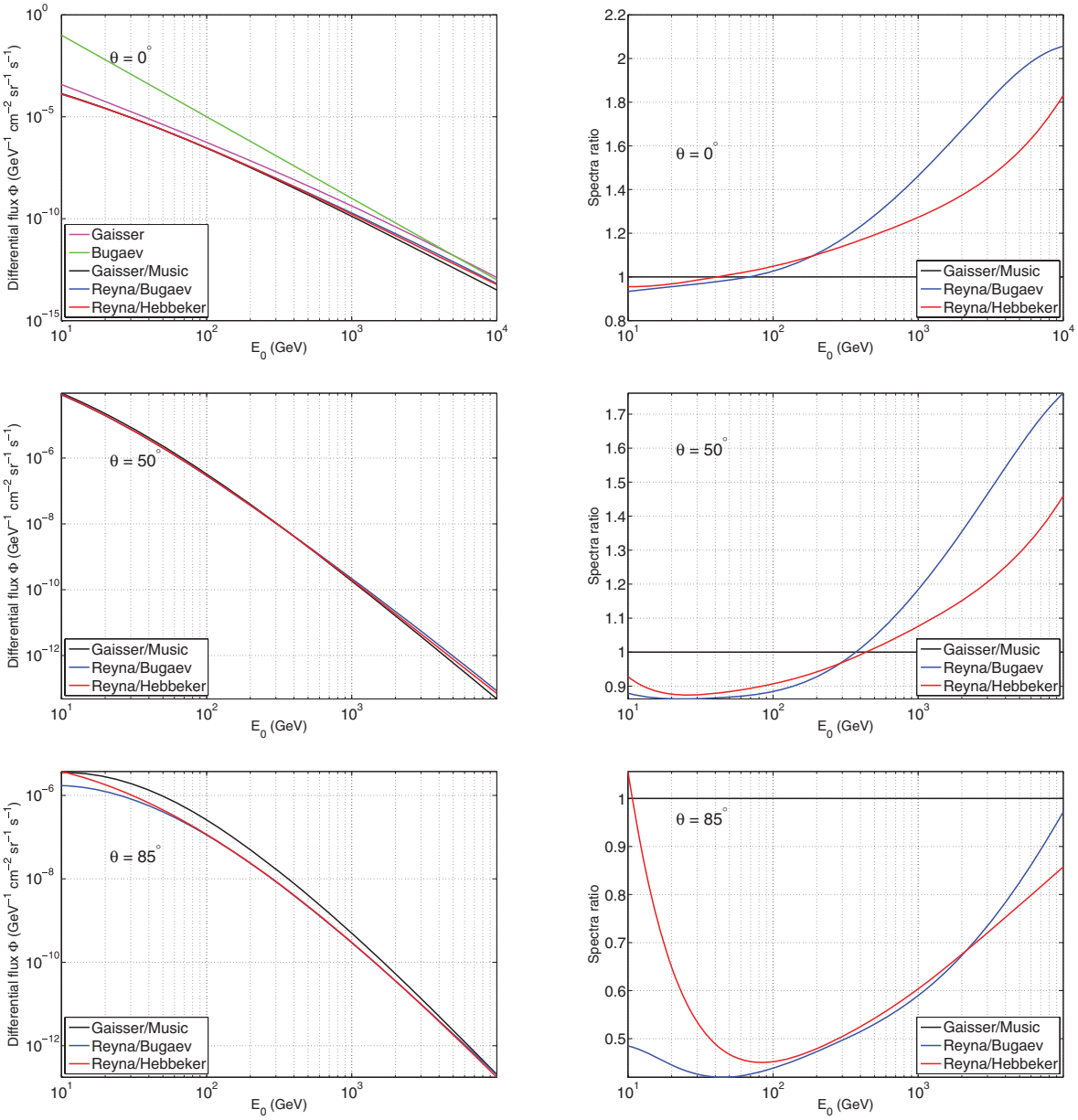

Figure 1. Left: differential spectra discussed in the present paper plotted for different zenith angles (see text for details). Right: spectra normalized with respect to the modified Gaisser spectrum (eqs 4–6).

for all zenith angles and for a wide range of sea level energy 1 GeV $\leq E_0 \leq$ 2000 GeV:

$$\Phi_{\rm R}(p,\theta) = \cos^3(\theta)\Phi_{\rm B}(p\cos\theta), \tag{11}$$

where $\Phi_{\rm B}$ is the Bugaev *et al.* (1998) spectrum given by eq. (7) but with $A_{\rm R} = 0.00253$, $\alpha_0 = 0.2455$, $\alpha_1 = 1.288$, $\alpha_2 = -0.2555$ and $\alpha_3 = 0.0209$. $\Phi_{\rm B}$ in (11) may be replaced by the $\Phi_{\rm H}$ spectrum of Hebbeker & Timmermans (2002) in eq. (9).

Fig. 1 shows the different spectra discussed in the present section for a range of energy E_0 and for zenith angle, θ, equal to $0^\circ, 50^\circ$ and 85°. For $\theta = 0^\circ$ the Bugaev spectrum strongly departs with unrealistic low-energy flux values up to three orders of magnitude larger than those predicted by the other four spectra. The Gaisser spectrum also predicts significantly larger values than the Gaisser–Music, Reyna–Bugaev and Reyna–Hebbeker spectra. These latter three spectra are remarkably grouped at low energy while the Gaisser–Music spectrum gives a lower flux in the high-energy domain. This behaviour remains for $\theta = 50^\circ$ but is no more observed for $\theta = 85^\circ$ where the three spectra give flux differing by a factor of 2 in the low-energy domain. For this high zenith angle, the Reyna–Hebbeker spectrum displays a spurious appearance at low energies.

In spite of the significant differences that can arise between each other, models of the second class are more suitable for a quick assessment of the muon imaging feasibility. Later in this paper (Section 6), we will show how the differences between the flux models in Fig. 1 affect the determination of the imaging conditions, through the proposed feasibility eq. (32).

2.2 Effects that may influence the muon flux

Some factors can induce either static (time-independent, locational) or dynamic (time dependent) effects on the observed muon flux.

Possible causes of static effects are altitude and geomagnetic latitude, while solar modulation and atmospheric variations may induce temporal fluctuations.

2.2.1 Altitude

The dependence of the muon flux on the altitude, driven by the changing distance between air shower cores and observation point, has been mainly investigated by comparing numerical results of simulation codes with data from balloon-borne experiments (Liu *et al.* 2003). In the latter, atmospheric muon spectra at different altitudes were measured through high-resolution superconducting spectrometers on board of balloons (e.g. Sanuki *et al.* 2002). Bellotti *et al.* (1996) and Hebbeker & Timmermans (2002) found that, for momenta above 10 GeV and altitudes within 1000 m a.s.l., a satisfactory interpolation of both numerical values and measured data is given by a relation of the form:

$$\frac{\Phi(h)}{\Phi(h=0)} = \exp(-h/h_0), \tag{12}$$

where h is the altitude (in m), while h_0 is an empirical characteristic length. According to Hebbeker & Timmermans (2002), $h_0 = 4900 + 750p$, with p being the muon momentum in GeV. Relying on (12), it results that, if the observation point is moved from the sea level to an altitude of 1000 m, a 5 (3) per cent increase in the flux will be observed, for a muon momentum of 20 (40) GeV.

2.2.2 Geomagnetic latitude

The geomagnetic field acts as a filter against low energy primary cosmic rays, when they propagate through the magnetosphere, down to Earth's atmosphere. Allowed primaries reach the atmosphere and produce secondary muons and neutrinos, while forbidden ones do not contribute to secondary fluxes. Thus, at any geomagnetic latitude, a cut-off rigidity (threshold) can be defined. The cut-off values are negligible at high geomagnetic latitudes (near the geomagnetic poles), while, at low latitudes, primary particles need to have a minimum rigidity to reach the atmosphere and this minimum value is higher for positive particles from the East than from the West. According to Cecchini & Sioli (2000), in the equator region the geomagnetic cut-off is about 15 GV and it causes an effect on the muon spectrum at sea level over momenta up to about 5 GeV.

2.2.3 Solar modulation

Variations in the solar wind velocity modulate the low energy spectrum of cosmic ray particles in the Earth's atmosphere. The dependence of the primary proton spectrum on solar activity follows the form (Bhattacharyya 1978):

$$P_0(E_p + C_p)^{-\gamma}, \tag{13}$$

where $P_0 \approx 1.8\,\mathrm{cm^{-2}\,sr^{-1}\,s^{-1}\,GeV^{\gamma-1}}$, $\gamma = 2.7$ and C_p varies from 1.8 during solar minimum to 3 for solar maximum. On the grounds of this parametrization, it results a 3 (1.6) per cent decrease in the primary proton flux at 50 (100) GeV, when passing from maximum to minimum solar activity. According to Bhattacharyya (1978) and Hebbeker & Timmermans (2002), this effect in the primary flux causes an uncertainty in the muon flux of 1 (10) per cent at a momentum of 10 (1) GeV. The uncertainty is proportionally lower at higher momenta.

2.2.4 Atmospheric variations

Variations in atmospheric conditions induce changes in the characteristics of the cosmic ray interactions and thus changes in muon intensity observed at the Earth's surface. In particular, changes in the temperature of the upper layers of atmosphere and hence changes in the air density, imply that a varying fraction of $\pi -$ mesons is captured by nuclei and thus a different number of pions decays into muons. The coupling between muon intensity variations and atmospheric temperature can be described by introducing the effective temperature, T_{eff}, that is, the weighted average of temperatures from the Earth's surface to the top of the atmosphere (Barrett *et al.* 1952, 1954; Ambrosio *et al.* 1997),

$$\frac{\Delta I}{I_0} = \alpha_T \frac{\Delta T_{\mathrm{eff}}}{T_{\mathrm{eff}}}, \tag{14}$$

where I_0 is the muon intensity obtained by integrating the flux Φ between the detector threshold and infinity and assuming an isothermal atmosphere. ΔI represents the fluctuations about I_0 and α_T is the depth-weighted temperature coefficient.

Through underground detectors (MACRO detector, in the Gran Sasso laboratory, Italy and IceCube observatory, deep in the Antarctic ice), Ambrosio *et al.* (1997) and Tilav *et al.* (2009) found, respectively, a ± 5 per cent and a ± 10 per cent seasonal fluctuation in the high energy muon rate. In both cases, the fluctuation in the muon rate was shown to be highly correlated with temperature variations in the stratosphere above the two observation points (± 5 and ± 10 K) and α_T was experimentally found to be equal to 0.9. According to Ambrosio *et al.* (1997), for zenith angles $\theta \approx 0$, α_T scales as,

$$\alpha_T = \left(1 + \frac{70}{p_{\mathrm{th}}}\right)^{-1}, \tag{15}$$

where p_{th} is the minimum momentum of the muon flux, I_0. Accordingly, the effect of atmospheric temperature is important only for muons with high energy.

The barometric effect on the muon flux is a consequence of the mass absorption of muons in the Earth's atmosphere: an increase of barometric pressure above the detector causes a greater absorption and thus a lower detection rate. While the temperature effect is determined by the temperature profile along the Earth's atmosphere, from its top to the detection level, the barometric effect is determined only by the pressure at the observation level.

The pressure coefficient, α_P, which relates changes in muon intensity to atmospheric pressure changes, depends on geomagnetic latitude (the coefficient is greater for detectors located at high latitudes), altitude of the observation point (it is greater at higher altitudes) and average energy of the particles (inverse proportionality). Values of α_P reported in the literature are of the order of -0.5 per cent $\mathrm{mbar^{-1}}$ for energies around 10 GeV. That implies negligible muon intensity fluctuations for standard atmospheric pressure changes (a few tens of mbar), even at low energies.

2.2.5 Relevance for geophysical muon imaging

Among the factors that induce time-independent effects on the muon flux, the altitude of the observation point may become relevant for geophysical muon imaging. In fact, over the lower energy part of the spectrum, a significant discrepancy might be found between measured and modelled flux, if the latter is referred to the sea level, while the experiment is carried out at high elevations (e.g. the summit zone of a large volcano, usually a few km a.s.l.). Conversely,

the geomagnetic cut-off can be disregarded since the effect it induces is small and influences only the lower energy part of the muon spectrum, likely below the threshold energy needed to cross even the smallest opacity of rock (see Section 3.1).

Among the factors that may induce time-dependent effects, the solar modulation can be disregarded because of (i) the relatively low amplitude of the fluctuations that it can cause on the muon flux and (ii) the period of its main component (11 yr), much longer than the return time of the geophysical phenomena that could be investigated through muon experiments. On the other hand, the seasonal fluctuation that the atmospheric temperature induces on the higher energy part of the muon spectrum may become important and thus it is to be taken into account, if muon radiographies are repeated at different times to identify time changes in the internal density distribution of the target object.

3 ATTENUATION OF THE MUON FLUX BY ROCK

3.1 Energy loss in matter

High-energies muons are relativistic particles which weakly interact with matter, mainly through ionisation (Adair & Kasha 1976). Bremβtrahlung, nuclear interactions and direct e^- e^+ pair production are the other physical processes by which muons loose energy. The loss of energy may be summarised by,

$$-\frac{\mathrm{d}E}{\mathrm{d}\varrho} = a(E) + b(E)E, \tag{16}$$

where a and b are functions depending on the material properties through which muons propagate. $\varrho(L)$ is the density integrated along the trajectory of the muons (see eq. 1) and the energy loss given by (16) is expressed in MeV g^{-1} cm^2.

The a function represents the energy loss due to ionisation, while b is for Bremβtrahlung, nuclear interactions and e^- e^+ pair production. The determination of these functions requires the computation of cross-sections and Monte Carlo modelling of interactions (Bugaev *et al.* 1998) and the main parameters influencing a and b are the average $\langle Z/A\rangle$ ratio and the bulk density of the material. In practice, computations may either be done with the general purpose software GEANT-4 or with computer programs dedicated to muon propagation through matter, like MUSIC (Kudryavtsev 2009), MMC or MUM (Sokalski *et al.* 2001).

Numerical values for a and b are provided by the Particle Data Group (http://pdg.lbl.gov), for a variety of materials and a wide range of energy. Fig. 2 shows the energy loss corresponding to the so-called standard rock ($\langle Z/A\rangle = 0.5$ and $\rho_{\mathrm{sr}} = 2650\,\mathrm{kg\,m^{-3}}$). When drawn in the log −log domain, the $\mathrm{d}E_{\mathrm{sr}}/\mathrm{d}\varrho$ curve varies smoothly and may be accurately fitted with a polynomial in a wide range of energy. Fig. 2 shows such a fit performed for $E_\mu \leq E \leq 1000$ GeV with a fourth-order polynomial and with a relative error never exceeding 2 per cent. This fit gives:

$$\frac{\mathrm{d}E_{\mathrm{sr}}}{\mathrm{d}\varrho} = -10^{l_4 y^4 + l_3 y^3 + l_2 y^2 + l_1 y + l_0}, \tag{17}$$

where $y = \log E$, with E in GeV and $l_4 = 0.0154$, $l_3 = -0.0461$, $l_2 = 0.0368$, $l_1 = 0.0801$, $l_0 = 0.2549$.

Excepted for rare instances, almost all types of rocks share the same $\langle Z/A\rangle$ ratio and the only varying quantity is the density. Consequently, the curves a_{sr} and b_{sr}, computed for the standard rock may safely be used to determine the attenuation of the flux of muons across all common rock types. Accordingly, in the remaining of the present paper, we shall use eq. (17) to compute the attenuation of the muon flux regardless of the kind of rock considered.

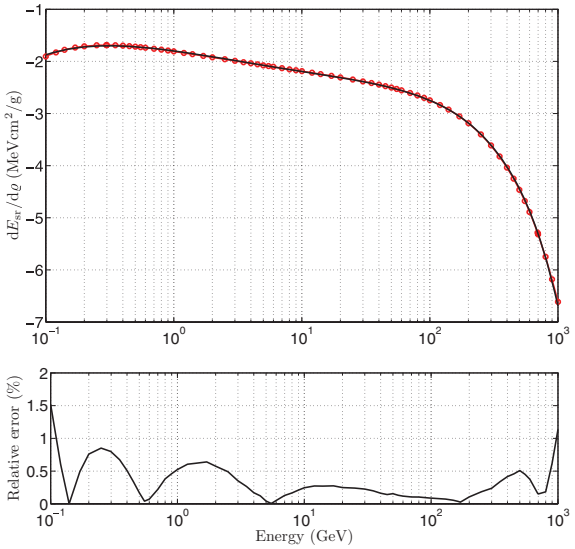

Figure 2. Top: energy loss for standard rock provided by the Particle Data Group (symbols) and fourth-order polynomial fit (solid line). Bottom: relative error between Particle Data Group values and polynomial approximation.

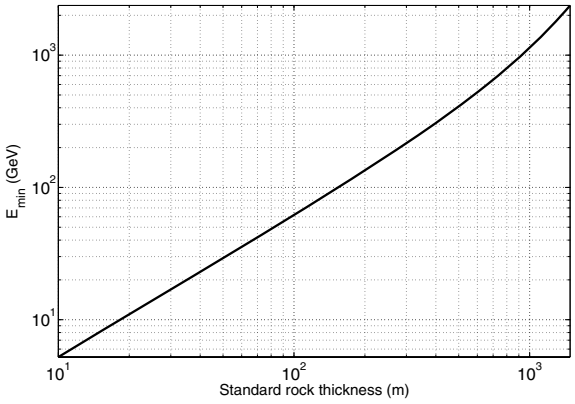

Figure 3. Minimum energy E_{min} [$\varrho(L)$] obtained by solving eq. (18) as a function of the standard rock thickness L.

By knowing the energy loss of muons across rock, it is possible to determine the minimum initial energy, E_{min}, necessary for a muon to cross a given opacity, ϱ_L, of rock before hitting the telescope. Practically, E_{min} is found by solving

$$E_{\mathrm{min}} - \int_0^{\varrho} \frac{\mathrm{d}E}{\mathrm{d}\varrho}\mathrm{d}\varrho = E_\mu, \tag{18}$$

where E_μ is the rest energy, whose value is given after eq. (8). Fig. 3 shows E_{min} as a function of the standard rock thickness. It can be observed that muons with energy as low as 30 GeV can be detected for rock thickness of about 50 m, as encountered on some geological situations (e.g. the Roselend site, discussed in Section 6). Under such conditions, Φ_0 models extending to the low-energy range are necessary.

The minimum energy, E_{min}, may then be used to compute the integrated flux,

$$I[\varrho, \theta] = \int_{E_{\mathrm{min}}(\varrho)}^{\infty} \Phi(E_0, \theta)\,\mathrm{d}E_0 \ (\mathrm{cm^{-2}\,sr^{-1}\,s^{-1}}). \tag{19}$$

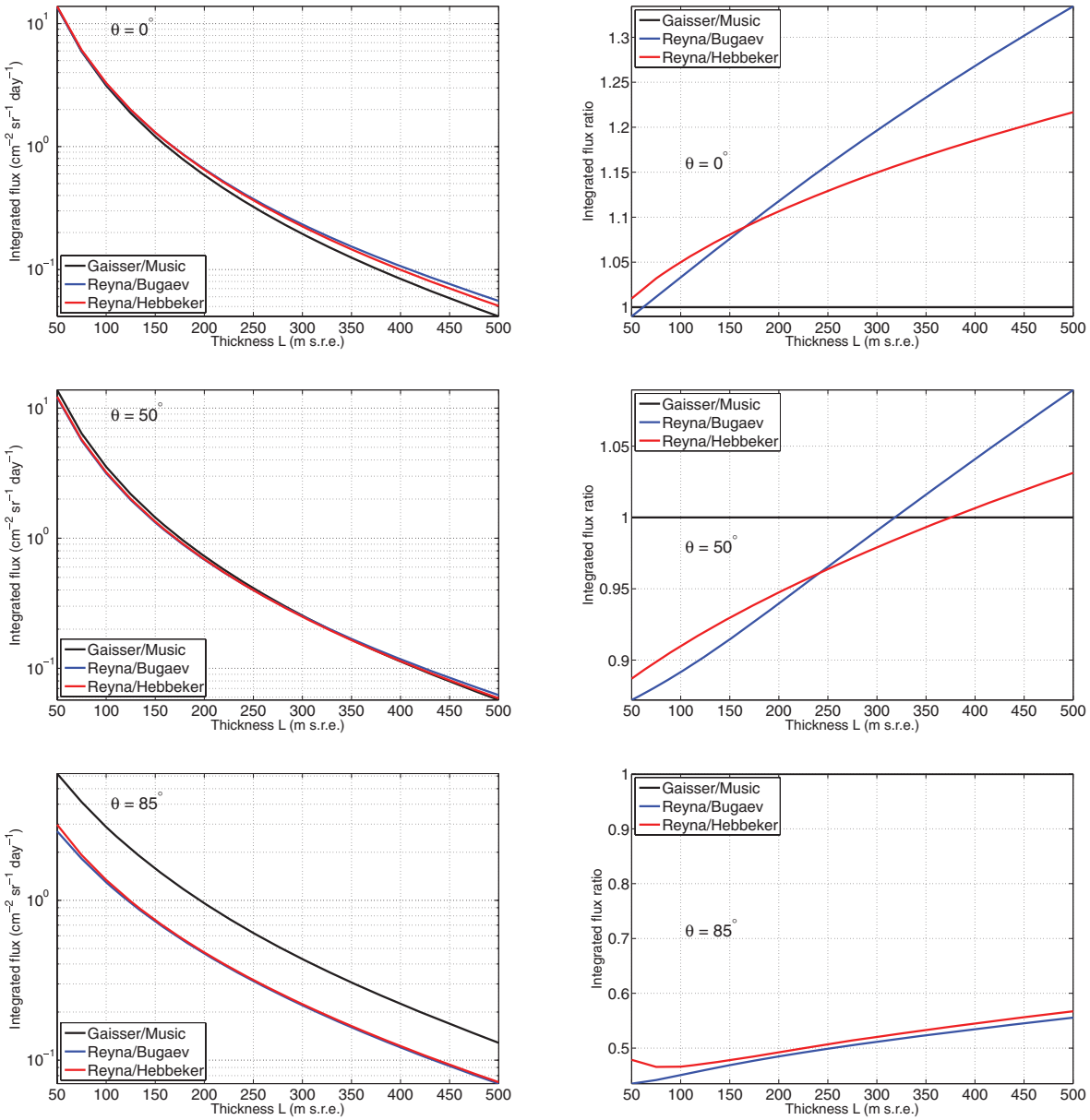

Figure 4. Left: integrated flux $I[\varrho(L), \theta = 0^\circ, 50^\circ, 85^\circ]$ (19) as a function of the standard rock thickness L expressed in standard rock equivalent metres (m s.r.e.). Right: integrated flux normalized with respect to the modified Gaisser spectrum (eqs 4–6).

Eq. (19) gives the time-average number of muons emerging from the geological body as a function of the opacity, ϱ.

Because of the power-law nature of the differential spectrum, $\Phi(E_0, \theta)$, the cut-off represented by the $E_{\min}$ limit results in a dramatic reduction of the output flux, $I[\varrho(L)]$. That is shown in Fig. 4, which represents the integrated flux computed for several zenith angles and for the Gaisser–Music, Reyna–Bugaev and Reyna–Hebbeker spectra. The similarities and differences observed in the spectra shown in Fig. 1 are retrieved in Fig. 4 and while both the Gaisser–Music and the Reyna–Bugaev flux appear very similar, the Reyna–Hebbeker significantly departs, especially at high zenith angles.

3.2 Scattering of muons

Despite their low cross-section, muons are continuously scattered along their travel-path across matter through Coulomb scattering with electrons. Indeed, this property is the one exploited in tomography of high-Z material (i.e. with many electrons) for nuclear waste detection (e.g. Jenneson *et al.* 2007; Stanley *et al.* 2008). An experimental study of muon scattering has been performed in the Fréjus experiment (Berger *et al.* 1989). Accounting for the random nature of scattering, the trajectories of the muons are deviated by an angle $\delta\theta$ from their original direction θ, with a probability given by a Rayleigh distribution:

$$P(\delta\theta) = \frac{\delta\theta}{\sigma_\theta^2} \exp\left[-\frac{\delta\theta^2}{2\sigma_\theta^2}\right]. \tag{20}$$

The Rayleigh parameter, σ_θ, is given by,

$$\sigma_\theta = \frac{\alpha}{E}\sqrt{\frac{\varrho}{\xi_0}}\left[1 + \kappa \ln \frac{\varrho}{\xi_0}\right], \tag{21}$$

where $\alpha = 13.6$ MeV, $\kappa = 0.038$. ξ_0 is the radiation length for standard rock, equal to 26.54 g cm^{-2}.

This equation shows that the scattering dispersion, σ_θ, of a muon hugely depends on its energy; consequently, it cannot directly be applied to long trajectories across rock, since muons loose energy along their paths. For such a situation, when a muon with $E > E_{\min}$ penetrates the rock, it scatters more and more while its energy decreases, according to (16). It is then necessary to integrate a differential form of eq. (21), combined with eq. (16), to obtain the total scattering dispersion. However, due to the E^{-1} dependence of σ_θ, most of the scattering occurs in the very last part of the trajectory where the muon energy is minimum.

As shown in Fig. 3, a minimum energy of 200 GeV is necessary for a muon to cross a rock layer of 300 m and, at this energy level, the scattering, σ_θ, is 0.53 mrad, after a 10 meter-long path. This scattering angle is negligible when compared to the angular resolution ∼50–100 mrad of our telescopes (see Section below). This is no more the case if we consider the last 10 metres of the trajectory where the muon energy is reduced by several GeV, leading to a scattering of 80 mrad. The net scattering dispersion may be obtained by summing the squared $\sigma_\theta{}'$s (i.e. the variances), computed along the muon trajectory, taking into account the energy loss. For the present example, we obtain a net dispersion $\hat{\sigma}_\theta = 50$mrad. This value is for the low-energy muons emerging from the rock and to obtain the total dispersion, we must further integrate (from $E_{\min}$ to ∞) the squared $\hat{\sigma}_{\theta\prime}$s, weighted by the differential energy spectrum. Pursuing with the present example where $L = 300$ m of standard rock, the total dispersion falls to ≈12 mrad. This values rises to ≈20 mrad for $L = 50$ m, since more low-energy muons are able to cross.

4 AN EXAMPLE OF MUON TELESCOPE

A central element in muon imaging experiments is the telescope. Its influence may be summarised by an acceptance function, $\mathcal{T}$, given in cm^2 sr and taking into account the geometrical characteristics of the instrument: the pixel size, the number of pixels and the distance between the matrices. In practise, the acceptance is the function by which the integrated flux is converted into a number, N, of muons:

$$N(\varrho) = \Delta T \times \mathcal{T} \times I(\varrho), \tag{22}$$

where the integrated flux, I, is given by eq. (19) and ΔT is the duration of the measurement period. Of course, the acceptance depends on the type of telescope and to give the reader an idea of what the $\mathcal{T}$ function may be, we now briefly describe the telescope we have designed to perform muon imaging experiments in the harsh conditions usually encountered in the summit zone of an active volcano. A complete description of our telescopes (Fig. 5) is given in Gibert *et al.* (2010) and in Lesparre *et al.* (2010). Another telescope with an acceptance similar to ours is described by Uchida *et al.* (2009).

Among the different detection systems available—emulsions (Tanaka *et al.* 2007b), resistive plate chambers (De Asmundis *et al.* 2007), micromegas (Giomataris *et al.* 2006), scintillators (Pla-Dalmau *et al.* 2001)—matrices made with scintillator strips are favoured by the teams doing experiments on volcanoes (Uchida *et al.* 2009; Gibert *et al.* 2010). This choice was also guided by the strong experience acquired by several authors of the present paper who participate to the OPERA experiment (Acquafredda *et al.* 2009). A detection matrix consists of two series of strips, aligned in the x and y directions and forming an array of pixels. A telescope is obtained by placing such matrices on the opposite faces of an imaginary parallelepiped, as shown in Fig. 5. A synoptic of the Ethernet Controller Module is given in the middle part of Fig. 5.

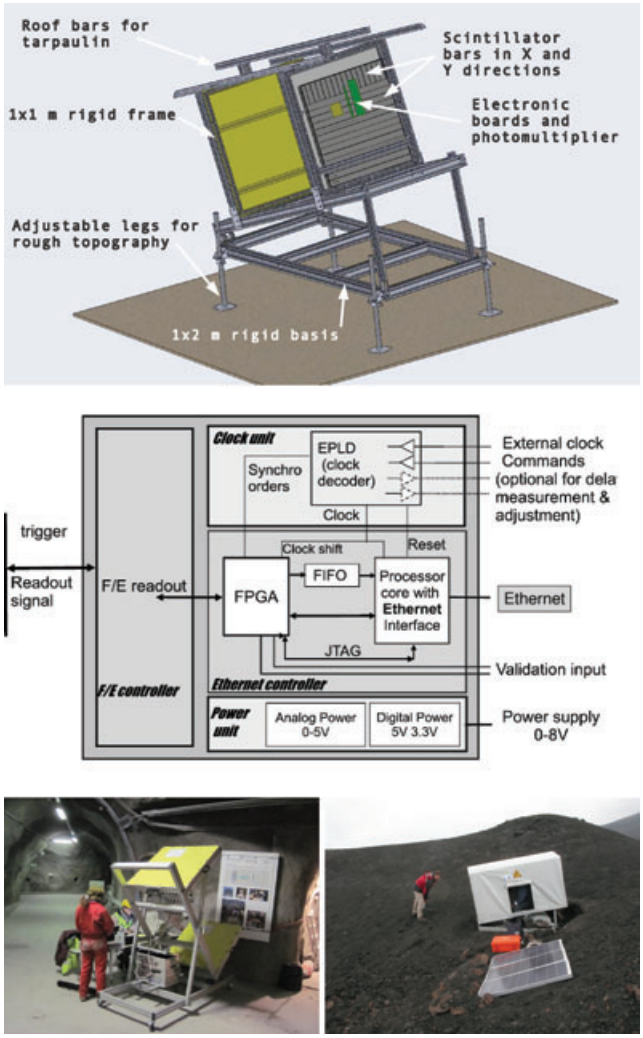

Figure 5. Top: general sketch of a small-size telescope. Bottom left: small-size telescope in operation in the Mont Terri underground laboratory. This telescope is equipped with two 16 × 16 matrices with 5^2 cm^2 pixels separated by $D = 120$ cm for this setup. Middle: sketch of the electronic mother board. Bottom right: another telescope, equipped with its protective tarpaulin and powered by solar panels, in operation near the South–East crater of Etna (Sicily) at an altitude of 3000 m.

This board ensures the coincident detection of events on X and Y bars of a matrix together with its dating with a 10 ns resolution. When an event is detected on one matrix, the acquisition software running on the central computer asks the other matrix to send an eventually synchronous event. If so, the event is recorded in the database for further post-processing.

The matrices of the telescope we designed are mounted on a modular aluminium frame which can be easily transported to the installation site and assembled in the field. The frame features adjustable legs, to cope with uneven terrains. It also features an upper structure that can rotate up to 90° with respect to a bottom frame structure, allowing precise orientation of the matrices toward the geological target. Waterproof cases house the matrices and all the other electronics. The above technical features allow our telescopes to be installed in extreme environmental conditions and where hosting facilities are not available as shown in the bottom-right part of Fig. 5. When a muon hits the matrices, the detection system records the front and the rear pixels flashed by ionisation and the direction of the muon trajectory can be determined.

The total solid angle, Ω, covered by the telescope and the angular resolution, $\delta\Omega$, depend on the number of pixels, $N_x \times N_y$, their size, d and the distance, D, separating the two matrices. $\delta\Omega$ covers all muon trajectories able to hit a given pair of pixels, $\{P^{\rm F}_{i,j}, P^{\rm R}_{k,l}\}$. All pairs of pixels with the same relative position, $\{m = i - k, n = j - l\}$, share the same average direction, $\mathbf{r}_{m,n}$ and the same $\delta\Omega(\mathbf{r}_{m,n})$ is assigned to all muons, whatever their actual trajectories. The direction $\mathbf{r}_{0,0}$ is normal to the matrices and corresponds to $N_{0,0} = N_x \times N_y$ pairs of homologue pixels $\{P^{\rm F}_{i,j}, P^{\rm R}_{i,j}\}$. For $\mathbf{r}_{m,n}$ with $\{m, n\} \neq \{0, 0\}$, $N_{m,n} < N_{0,0}$ and the larger the shifts m and n, the smaller $N_{m,n}$. Consequently, the directions near $\mathbf{r}_{0,0}$ have a large detection area (i.e. number of pairs of pixels) and those departing too much have a negligible one. The acceptance is obtained multiplying the detection area by the angular resolution,

$$\mathcal{T}(\mathbf{r}_{m,n}) = S(\mathbf{r}_{m,n}) \times \delta\Omega(\mathbf{r}_{m,n}). \tag{23}$$

A telescope with two matrices of $N_x \times N_y$ pixels has $(2N_x - 1) \times (2N_y - 1)$ discrete directions, $\mathbf{r}_{m,n}$, spanning Ω. For instance, the telescope of Fig. 5 has 961 discrete directions. The upper part of Fig. 6 shows the angular resolution, $\delta\Omega(\mathbf{r}_{m,n})$, for this telescope with $N_x = N_y = 16$, $d = 5$ cm and $D = 80$ cm. The total angular aperture of the telescope is roughly $\pm 30^\circ$, as can be seen on the X and Y axes of Fig. 6. The acceptance $\mathcal{T}(\mathbf{r}_{m,n})$ is shown in the bottom part of Fig. 6 and as expected, the largest detection surface corresponds to the normal direction, $\mathbf{r}_{0,0}$ and reaches $\simeq 25$ cm^2 sr in this example. The acceptance is almost zero for a margin corresponding to the directions which most depart from $\mathbf{r}_{0,0}$ and only a fraction of all possible directions of detection will be efficient. Accounting for this effect, the total angular aperture of the telescope is actually restricted to a cone of 15° around $\mathbf{r}_{0,0}$.

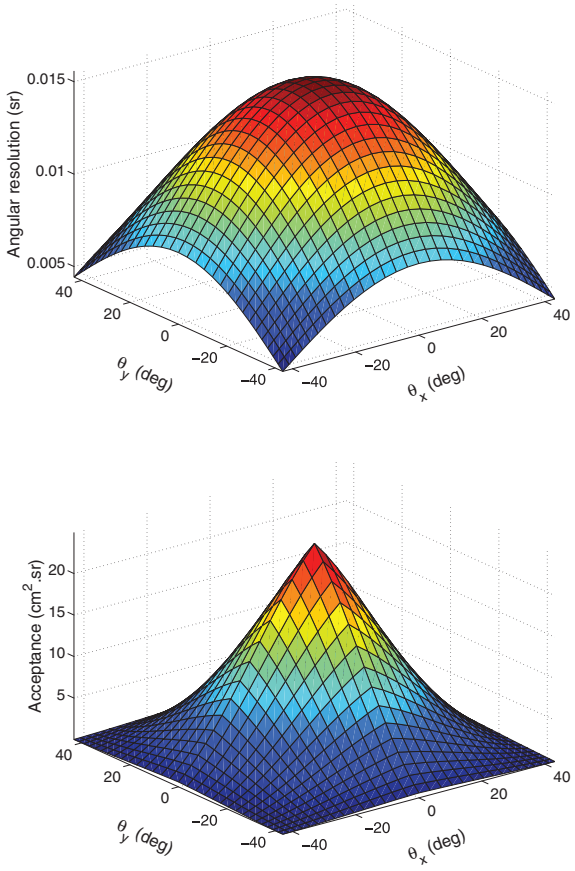

Figure 6. Azimuthal angular properties of the telescope of Fig. 5 equipped with two 16×16 matrices with pixel size $d = 5$ cm and separated by $D = 80$ cm as for the data shown in Fig. 7. Top: Angular resolution $\delta\Omega(\mathbf{r}_{m,n})$ for each discrete direction of sight $\mathbf{r}_{m,n}$ of the pair of matrices. Bottom: Acceptance $\mathcal{T}(\mathbf{r}_{m,n})$.

Besides the telescope shown in Fig. 5 we plan to produce another one differing only in the number of pixel: $N_x = N_y = 32$ and $d = 5$ cm. Depending on its geometrical configuration, this telescope can have an acceptance up to ≈ 250 cm^2 sr for an angular resolution not exceeding 0.03 sr. However, such a large telescope probably represents the upper limit of what can be done for instruments being installed on rough topography through helicopter hauling. For comparison, the telescope described by Uchida *et al.* (2009) has $N_x = N_y = 12$ and $d = 7$ cm. For $D = 100$ cm this gives $\mathcal{T} \approx 30$ cm^2 sr and an angular resolution less than 0.018 sr.

5 EXPERIMENTAL CONDITIONS FOR MUON IMAGING

We now use the results obtained in the preceding Sections to establish a link between the data, that is, the number, N, of muons recorded during a given amount of time, ΔT, the telescope acceptance, $\mathcal{T}$ and the physical parameter $\varrho(L)$. Taking an acceptance of 15 cm^2 sr (Fig. 6) and the I-curve of Fig. 4, we find that N may be as high as 1000 muons per day for a rock thickness $L \approx 100$ m or as low as 1 muon per day for $L \approx 1000$ m. An important issue is to determine the experimental conditions that must be satisfied to be able to distinguish two nearby opacities, ϱ_0 and $\varrho_0 + \delta\varrho$, or, equivalently, to statistically make the difference between $N(\varrho_0)$ and $N(\varrho_0 + \delta\varrho)$. Starting from (22) and using (19), we have:

$$\Delta N(\varrho_0, \delta\varrho) \equiv N(\varrho_0 + \delta\varrho) - N(\varrho_0) \tag{24}$$

$$= \Delta T \times \mathcal{T} \times \left.\frac{{\rm d}I(\varrho)}{{\rm d}\varrho}\right|_{\varrho=\varrho_0} \delta\varrho \tag{25}$$

$$= \Delta T \times \mathcal{T} \times \Delta I(\varrho_0, \delta\varrho), \tag{26}$$

with

$$\Delta I(\varrho_0, \delta\varrho) = \Phi[E_{\rm min}(\varrho_0)] \times \left.\frac{{\rm d}E_{\rm min}}{{\rm d}\varrho}\right|_{\varrho=\varrho_0}. \tag{27}$$

Let δN be the half-width of the confidence interval assigned to the measured number of muons $N(\varrho_0)$. The opacity variation $\delta\varrho$ will be resolvable if,

$$\Delta N(\varrho_0, \delta\varrho) = \Delta T \times \mathcal{T} \times \Delta I(\varrho_0, \delta\varrho) > \delta N. \tag{28}$$

Assuming that the sequence forming the N detected events is described by a Poissonian process with constant rate N, the central confidence interval, $[N_l, N_u]$, at probability level $1 - \alpha$, is such that:

$$\sum_{n=0}^{N_l} \frac{N^n {\rm e}^{-N}}{n!} = \sum_{n=N_u}^{\infty} \frac{N^n {\rm e}^{-N}}{n!} = \frac{\alpha}{2}. \tag{29}$$

Since the Poissonian distribution is defined on the set of positive whole numbers, the equalities (29) may not be satisfied exactly and several intervals with the same confidence level can sometimes be obtained (Conrad *et al.* 2003).

For large enough N (say $N > 50$), the Poissonian distribution may be reasonably approximated by a Gaussian with mean N and standard deviation $\sqrt{N}$. However, the so-called continuity correction, $n \to n + 0.5$, must be applied to the Gaussian variable, to account

for the fact that the Poissonian distribution is defined only for integer values, while the Gaussian is for real variables. In practise, we have:

$$\frac{N^n \mathrm{e}^{-N}}{n!} \approx \frac{1}{\sqrt{2\pi N}} \exp\left(-\frac{(n+0.5-N)^2}{2N}\right). \quad (30)$$

When the Gaussian approximation holds, the confidence interval is obtained through standard procedure and we have $\delta N = 2\sqrt{N}$ for $1-\alpha = 0.95$ and $\delta N = \sqrt{N}$ for $1-\alpha = 0.68$. For this latter case, condition (28) gives,

$$\Delta T \times \mathcal{T} \times \Delta I(\varrho_0, \delta\varrho) > \sqrt{N}. \quad (31)$$

Using expression (22) this equation rewrites as,

$$\Delta T \times \mathcal{T} \times \frac{\Delta I^2(\varrho_0, \delta\varrho)}{I(\varrho_0)} > 1. \quad (32)$$

The equation above represents the feasibility condition, the main focus of the present study, allowing to define the applicability domain of muon imaging. Through this relation it is possible to test the suitability of the method to investigate the density distribution inside some candidate target structures. The left-hand term of condition (32) is determined both by the fixed total opacity of the medium, which depends on the characteristics of the geological target and by the desired resolution level $\delta\varrho$. This sets the minimum value for the product $\Delta T \times \mathcal{T}$ and the question is to determine whether it is reachable or not. This will clearly depend on the particular constrains attached to a given experimental situation. For instance, one can easily imagine experiments where both the acceptance of the telescope (i.e. its size) and the duration of the measurement period cannot exceed some limits. In such a case, eq. (32) will fix the minimum value for $\delta\varrho$.

6 DISCUSSION OF SOME GEOLOGICAL SITUATIONS

We now present some experimental conditions, corresponding to possible applications of muon imaging on the field. In particular, we consider the Mont Terri and Roselend underground laboratories and La Soufrière and Mt. Etna volcanoes.

6.1 Underground laboratories

The Mont Terri underground laboratory (Switzerland) is located in an anticline formed with layers of Opalinus clay and limestones with densities $\rho_{\mathrm{clay}} = 2.4$ and $\rho_{\mathrm{lime}} = 2.7$ (Bossart & Thury 2008). The thickness of the geological cover varies from 250 to 500 m, depending on the topography of the mountain (Fig. 7) and on the inclination of the telescope presently in operation on this site (Fig. 5). The laboratory is at an altitude of 500 m and the top of the mountain is at ≈900 m. Taking a zenith angle of 0° and an average thickness, L, of 400 m, equally divided between clay and limestone, we obtain an integrated flux $I = 0.2516\,\mathrm{cm}^{-2}\,\mathrm{sr}^{-1}\,\mathrm{day}^{-1}$ in good agreement with the data (bottom part of Fig. 7). The discrepancy between the experimental and the synthetic curves may safely be attributed to variations if the geological structure. The structure of the Mont Terri is such that its geometry is invariant in a direction parallel to the axis of the anticline. In such particular circumstances, the telescope may be reconfigured by merging its pixels along the direction parallel to the anticline axis. By doing so, the effective acceptance of the telescope is magnified while the angular resolution is reduced in the same proportions. In the experiment presently discussed, pixels were merged by groups of seven,

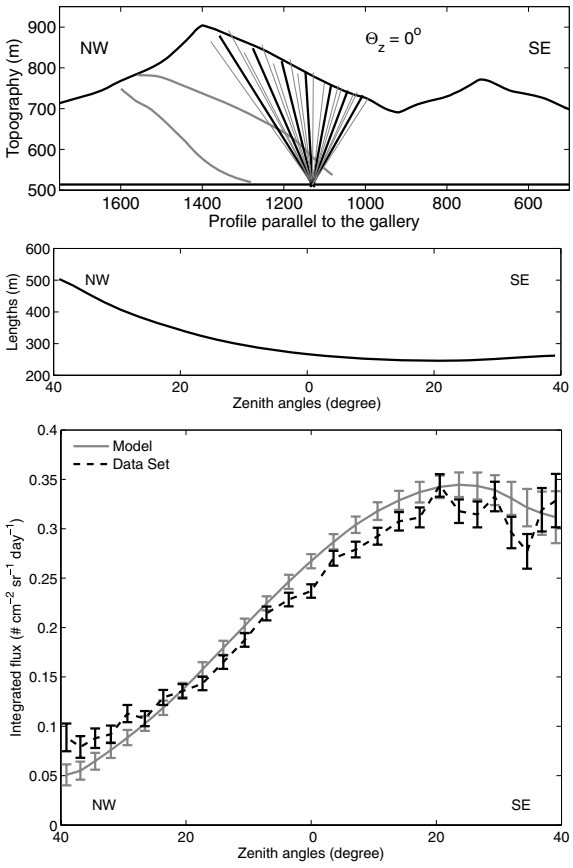

Figure 7. Mont-Terri experiment—Top: cross-section showing the topography profile of the Mont-Terri mountain above the underground laboratory. The fan-like rays symbolise the angular coverage of the telescope. The curved thin line represent the interface between geological layers. Middle: ray length as a function of the zenith angle. Bottom: muon flux recorded by the telescope during one month with $\pm 1\sigma$ error bars. Also shown is the theoretical integrated flux I (eq. 19).

leading to an acceptance, $\mathcal{T}$, of about 100 cm^2 sr. Let us suppose that we want to detect a variation of ±10 m in the position of the interface between clay and limestone, over a total thickness of 300 m. Depending on the flux model retained, the flux variation varies from 0.00479 to 0.00531 $\mathrm{cm}^{-2}\,\mathrm{sr}^{-1}\,\mathrm{day}^{-1}$ with corresponding $I = 0.2199$ and $0.2610\,\mathrm{cm}^{-2}\,\mathrm{sr}^{-1}\,\mathrm{day}^{-1}$. Using these values, eq. (32) gives $\Delta T > 90$–96 days at the 1σ confidence level.

The Roselend underground laboratory (French Alps) offers very different conditions from those encountered at the Mont Terri site, with a thickness, L, of the geological cover varying from 10 to 50 m, depending both on the location along the gallery and on the inclination of the telescope. This gives a much larger integrated flux I comprised between 13 and $185\,\mathrm{cm}^{-2}\,\mathrm{sr}^{-1}\,\mathrm{day}^{-1}$ for $\rho = 2.7$ g cm^{-3}. For a density variation $\delta\rho = 0.01$ g cm^{-3} the fluctuation ΔI varies from 0.098 to $0.848\,\mathrm{cm}^{-2}\,\mathrm{sr}^{-1}\,\mathrm{day}^{-1}$. To resolve this density variation with $\mathcal{T} \approx 20$ cm^2 sr, eq. (32) gives a duration ΔT comprised between 13.5 ±1 and 72 ±2 days, where the uncertainties are obtained from the different flux models used.

6.2 Volcanoes

La Soufrière of Guadeloupe is an andesitic volcano whose lava dome is about 500 yr old (Boudon *et al.* 2008) and which presents a

diversified number of hazards including phreatic eruption, flank collapse and explosive magmatic eruption (Komorowski *et al.* 2008). Using electrical resistance tomography, Nicollin *et al.* (2006) found that the lava dome is highly heterogeneous, with massive lava volumes embedded in more or less hydrothermalized materials. Knowing the internal structure of the dome is an important issue because of its implications on flank-destabilization models. For this reason, La Soufrière is a priority target for muon imaging (Gibert *et al.* 2010). Gravity data measured on and in the vicinity of the volcano show that the local bulk density varies from 2.2 to 2.7 g cm^{-3} (Gunawan 2005). However, densities as low 1.5 g cm^{-3} may be encountered.

One expected site for a telescope is located at the Col de l'Échelle, on the Eastern side of the volcano. This place is particularly interesting since there is no topographic high present behind the lava dome (i.e. on its western side) to produce perturbing shadow effect. To embrace the whole volcano in a single view, the telescope must have an effective horizontal aperture angle of 90° and zenith angles comprised between 55° and 90°. Accounting for the fact that the extreme angles are useless (top part of Fig. 6), this fixes the matrix distance $D = 80$ cm and the maximum acceptance $\mathcal{T} \approx 20$ cm^2 sr (bottom part of Fig. 6). The thickness, L, of rock varies from tens of meters at the summit to about 800 m at the base of the volcano and the corresponding integrated flux, I, is comprised between 0.01 and 10 cm^{-2} sr^{-1} day^{-1} for a mean density $\rho = 2.2$ g cm^{-3} (Fig. 8). Let us consider a volume of massive andesite (2.7 g cm^{-3}) with a diameter of 100 m embedded in altered rock (2.2 g cm^{-3}). Taking a total ray length $L = 550$ m and a zenith angle $\theta = 70°$ we obtain an integrated flux $I \approx 0.09$ cm^{-2} sr^{-1} day^{-1} for both Reyna models and of $I \approx 0.11$ cm^{-2} sr^{-1} day^{-1} for the Gaisser/Music model. This difference, not seen for the Mont Terri and Roselend simulations, come from the fact that the Gaisser/Music flux significantly differs from the other two models at high zenith angles (Fig. 4). Similarly, depending on the model chosen, the flux variation ΔI varies from ≈ 0.010 to ≈ 0.012 cm^{-2} sr^{-1} day^{-1}. Taking an acceptance, $\mathcal{T}$, of 20 cm^2 sr, eq. (32) gives a duration $\Delta T > 37$–50 days.

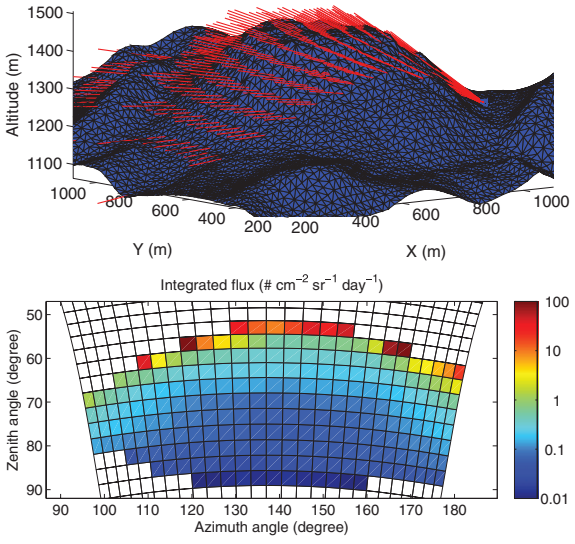

Figure 8. La Soufrière of Guadeloupe model–Top : model of topography in blue, the telescope is located at Col de l'Échelle, the red rays represent some of the muons trajectory across the volcano detected by a 16 × 16 pixels telescope with a distance between matrices of 80 cm. Bottom: the integrated flux of each trajectory passing through the volcano.

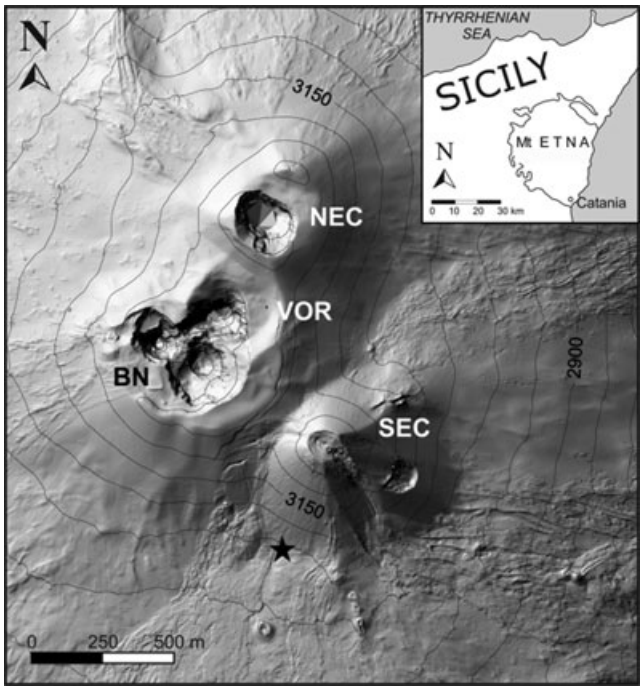

Figure 9. Sketch map of the summit zone of Mt. Etna (topographic map by Favalli *et al.* 2009) showing the position of the four Summit Craters (NEC = Northeast Crater, VOR = Voragine, BN = Bocca Nuova, SEC = South–east Crater). The black star marks the planned installation site for the muon telescope. The inset at the top right shows the location of Mt. Etna with respect to Sicily (Italy).

Mt. Etna is a large (1200 km^2) strato-volcano sited on the East coast of Sicily (Italy). It has a base diameter of about 40 km and a height of about 3350 m. The scale of this volcano implies that, at the current state of the art, only a small portion of its edifice can be investigated through muon imaging. In fact, to have a sufficient flux, the thickness of rock to be crossed by muons should not exceed a few kilometers and the time interval needed to resolve a given density contrast, using a mobile detector of limited dimensions, should not exceed the typical period of volcanic processes able to change the internal density distribution of the target structure. One of the active craters in the summit area of the volcano would be a suitable target for the first experiment of muon radiography at Mt. Etna. In particular, the Southeastern Crater would be the more appropriate due to both its size and position. This crater is about 240 m tall (from 3050 to 3290 m a.s.l.), with a base diameter of about 500 m (Fig. 9). Simulations we carried out show that a good installation point for a muon telescope is located on the southern slope of the crater. This point is easily reachable from the dirt track road that crosses the summit zone of the volcano.

Muon rays crossing the middle part of Etna's South–east crater to reach a detector placed at its base, would have a zenith angle of about 68° and would cross about 500 m of rock. This imply a flux of 0.085 cm^{-2} sr^{-1} day^{-1}, assuming an average density of the crater of 2.5 g cm^{-3}. Let us assume we perform a muon radiography experiment during the period when the summit zone of Etna is free from the snow cover (roughly June–October, $\Delta T \approx$ 150 days). Using eq. (32) and assuming that $\mathcal{T}$ is 15 cm^2 sr, it results a minimum ΔI of 0.006 cm^{-2} sr^{-1} day^{-1}. This result can be converted into the minimum resolvable opacity change, $\delta\varrho$, which results to be equal to 1.5×10^3 g cm^{-2}. Thus, an inner structure with size exceeding the space resolution of the telescope (about

10 m, assuming a 500 m distance to the target and corresponding to an angle of 20 mrad) will be recognized if the density contrast is at least 0.5 g cm^{-3}. Larger inner structures will need proportionally smaller density contrasts in order to be recognized. In any case, even if inner structures have size of the order of a few tens of meters, density contrasts close to 0.5 g cm^{-3} are likely to be encountered if a part of the crater is filled with a low density foamy magma. Hence, as already found by Tanaka *et al.* (2009a), detailed info on the inner architecture (presence and position of conduits, chambers, etc.) and functioning (e.g. convective recycling of degassed magma) of the crater could be retrieved through muon imaging. It is worth stressing that the effect of altitude on the energy spectrum of muons arriving on the summit zone of Etna (above 3000 m a.s.l.) is to be taken into account (see Section 2.2.1).

7 CONCLUSIVE REMARKS

We comprehensively discuss the constraints on geophysical imaging using cosmic muons. In our study we take into account the three key elements involved in muon imaging for Earth Sciences purposes, namely: (i) the characteristics of the flux of incident cosmic muons, (ii) the attenuation of the muon flux by rock and (iii) the geometrical characteristics of the detector. The intersection of the constraints imposed by each of these three elements determine the feasibility of muon imaging, under a given set of geological conditions.

The choice of a suitable model describing the flux of incident cosmic muons is of primary importance since errors in the incident flux will be propagated to the resulting density distribution inside the target object. In the case of real applications in the field, the flux of incident cosmic muons should be assessed in the measurement site, through an acquisition in open sky conditions, before turning the telescope towards the target object. The so-obtained experimental integrated flux can be used to both determine the correction function to apply to the telescope theoretical acceptance and to re-normalize the flux model used to compute the flux attenuation produced by the geological target. In the framework of a feasibility study, theoretical models must be used. Ideally, the differential flux of muon should be derived through a full Monte Carlo simulation (e.g. CORSIKA; Heck *et al.* 1998). However, for the sake of a quick assessment of the muon imaging feasibility, it is advisable to utilise more manageable tools. Many authors have proposed empirical parameter curves to fit observed muon flux data (e.g. Gaisser 1990; Bugaev *et al.* 1998; Hebbeker & Timmermans 2002; Reyna 2006; Tang *et al.* 2006). Nonetheless, in spite of the large amount of measured data, there exist significant discrepancies between the different proposed parametrizations. For example, we have shown that, at low energies, the model proposed by Bugaev *et al.* (1998) overestimates the flux by up to three orders of magnitude with respect to the other four models considered. This difference is especially significant when the density distribution inside thin layers of rock is to be investigated and thus even low energy particles contribute to the integrated flux. Naturally, these differences imply an incertitude when defining the feasibility conditions of the muon imaging, in a given geological situation, as shown in the previous section. Moreover, we show that both the elevation of the observation point and the atmospheric temperature may induce relevant effects on the muon flux that should be taken into account.

The loss of energy that muons undergo when they travel through rock (due to ionization and other interactions) is usually determined through further Monte Carlo modelling (e.g. GEANT or MUSIC; Kudryavtsev 2009), which considers the possible interactions, including muon-nucleus inelastic scattering. However, we show that, using the numerical values provided by the Particle Data Group, an equation can be obtained describing, with sufficient accuracy, the attenuation of the muon flux, as a function of the crossed opacity. In practise, the proposed equation allows to retrieve the minimum initial energy, $E_{\min}$, that a muon needs to cross a given opacity of rock. $E_{\min}$ is then used as the lower limit of integration to compute the time-average number of muons crossing the target object, starting from the equation of the incident flux.

We have designed a muon detector (under production at the time of this writing) which can work outdoor, even under the hash conditions that may be encountered when performing geophysical campaigns (e.g. in the summit zone of an active volcano). Thanks to a modular mounting frame, the telescope can be easily transported and when assembled in the field, can cope with uneven terrains and can be precisely oriented towards the target object. The detection system is based on plastic scintillator bars, forming two matrices at a given distance and the timing and direction of the hitting muon is retrieved by recording the pixels flashed by ionization in the two matrices. The geometrical characteristics of the telescope (pixel size, number of pixels, distance between the two matrices) determine the acceptance, the function by which the integrated flux is converted into a number of muons.

After discussing the three above key elements, we propose a feasibility equation relating (i) the duration of the muon experiment, (ii) the acceptance of the telescope, (iii) the integrated flux of muons and (iv) the variation in the integrated flux caused by a structure inside the target object, with different density than the surrounding rock. By means of this relation it is possible to delineate a domain of applicability of the muon imaging, in different geological situations. For example, using our results, we show that, after 50 to 150 days of data acquisition, it is possible to distinguish, inside target objects with size of some hundreds of meters and at the 1- σ confidence level, inner structures with size of 20–100 m, if they have a density contrast of the order of 0.5 g cm^{-3} with respect to the surrounding material. Such density contrasts can be found inside above-ground volcanic structures due to, for example, different alteration degree of the rock or presence of conduits filled with low density foamy magma. Thus, even after relatively short observation periods, muon imaging can supply valuable information about the internal structure of a volcano.

Our study is broadly relevant to other research groups as it provides the tools to assess the space/density resolution capabilities of muon imaging, in the allocated time slot and under the conditions imposed by a given geological situation.

ACKNOWLEDGMENTS

This paper is dedicated to the memory of our friend and colleague Albert Tarantola who participated with us to the launch of the DIAPHANE muon tomography project. H. Tanaka and an anonymous referee made very constructive reviews of a former version of the paper. The design and the construction of the telescopes greatly benefited from the skilled expertise of Bruno Carlus (computer), Bruno Kergosien (electronics), Pascal Rolland (mechanical engineering) and Sylvain Vanzetto (optical fibres). The DIAPHANE project is financially supported by the IPGP (www.ipgp.fr) BQR grant, the DOMOSCAN ANR (www.agence-nationale-recherche.fr) project, the CNRS/IN2P3 (www.cnrs.fr) Astroparticles program and the Muon Densitometry (MD) experiment funded by Swisstopo and CRIEPI partners of the Mont Terri project (www.mont-terri.ch). Daniele Carbone benefited from a 6-months sabbatical stay in IPGP funded

by the Research in Paris grant program (www.paris.fr). This is IPGP contribution 3065.

REFERENCES

Acquafredda, R. & the OPERA Collaboration, 2009. The OPERA experiment in the CERN to Gran Sasso neutrino beam, *JINST,* **4,** P04018, doi:10.1088/1748-0221/4/04/P04018.

Adair, R.K. & Kasha, H., 1976. in *Muon Physics,* Vol. 1, p. 323, eds Hughes, V.W. & Wu, C.S., Academic Press, New York.

Aglietta, M. & the, LVD Collaboration, 1999. Upper limit on the prompt muon flux derived from the LVD underground experiment, *Phys. Rev. D,* **60,** 112001.

Alvarez, L.W. *et al.*, 1970. Search for hidden chambers in the pyramids, *Science,* **167,** 832–839.

Ambrosio, M. & the, MACRO Collaboration, 1997. Seasonal variations in the underground muon intensity as seen by MACRO, *Astropart. Phys.,* **7,** 109–124.

Auger, P., 1941. *Les rayons cosmiques,* 136 pp., PUF, Paris.

Barrett, P.H., Bollinger, L.M., Cocconi, G., Eisenberg, Y. & Greisen, K., 1952. Interpretation of cosmic-ray measurements far underground, *Rev. Mod. Phys.,* **24,** 133–178.

Barrett, P., Cocconi, G., Eisenberg, Y. & Greisen, K., 1954. Atmospheric temperature effect for mesons far underground, *Phys. Rev.,* **95,** 1573–1575.

Berger, Ch. & the, Fréjus Collaboration, 1989. Experimental study of muon bundles observed in the Fréjus detector, *Phys. Rev. D,* **40,** 2163–2171, doi:10.1103/PhysRevD.40.2163.

Bhattacharyya, D.P., 1978. Effect of solar modulation on the low energy sea level muon spectrum near the geomagnetic equator, *Aust. J. Phys.,* **31,** 451–453.

Bellotti, R. *et al.*, 1996. Measurement of the negative muon spectrum between 0.3 and 40 GeV/c in the atmosphere, *Phys. Rev. D,* **53**(1), 35–43.

Bossart, P. & Thury, M. (eds), 2008. Mont Terri Rock laboratory project, Programme 1996 to 2007 and Results, Rep. Swiss Geological Survey 3, Wabern, Switzerland.

Boudon, G., Komorowski, J.-C., Villemant, B. & Semet, M.P., 2008. A new scenario for the last magmatic eruption of La Soufrière of Guadeloupe (Lesser Antilles) in 1530 A.D. Evidence from stratigraphy radiocarbon dating and magmatic evolution of erupted products, *J. Volcanol. Geotherm. Res.,* **178,** 474–490, doi:10.1016/j.jvolgeores.2008.03.006.

Bugaev, E.V., Kotov, Yu D. &Rosental, I.L., 1970. *Cosmic Muons and Neutrinos,* Atomizdat, Moscow.

Bugaev, E.V., Misaki, A., Naumov, V.A., Sinegovskaya, T.S., Sinegovsky, S.I. & Takahashi, N., 1998. Atmospheric muon flux at sea level, underground, and underwater, *Phys. Rev. D,* **58,** 054001.

Cecchini, S. & Sioli, M., 2000. Cosmic ray muon physics, preprint, arXiv:hep-ex/0002052v1.

Conrad, J., Botner, O., Hallgren, A. & Pérez de los Heros, C., 2003. Including systematic uncertainties in confidence interval construction for Poisson statistics, *Phys. Rev. D,* **67,** 012002.

Crozon, M., 2005. *Quand le ciel nous bombarde,* 246, pp., Vuibert, Paris.

De Asmundis, R., Avella, P. & Toglia, F., 2007. Using RPC detectors as cosmic rays monitors, *IEEE Trans. Nucl. Sci.,* **54,** 670–676, doi:10.1109/TNS.2007.895505.

Favalli, M, Fornaciai, A. & Pareschi, M.T., 2009. LiDAR strip adjustment: application to volcanic areas, *Geomorphology,* **111,** 123–135, doi:10.1016/j.geomorph.2009.04.010.

Gaisser, T., 1990. *Cosmic Rays and Particle Physics,* Cambridge University Press, New York.

Gaisser, T. & Stanev, T., 2008. Cosmic Rays, *Phys. Lett. B,* **667,** 254–260, doi:10.1016/j.physletb.2008.07.028.

Gibert, D., Beauducel, F., Déclais, Y., Lesparre, N., Marteau, J., Nicollin, F. & Tarantola, A., 2010. Muon tomography: plans for observations in the Lesser Antilles, *Earth Planets Space,* **62,** 153–165.

Giomataris, I. *et al.*, 2006. Micromegas in a bulk, *Nuclear Instrum. Methods A,* **560,** 405–408.

George, E.P., 1955. Cosmic rays measure overburden of tunnel, *Commonwealth Engineer,* 455–457.

Gunawan, H., 2005. Gravity and microgravity applied to volcanology: examples of La Soufrière of Guadeloupe and of Merapi (Indonesia), *PhD thesis*, IPG Paris (in French).

Hebbeker, T. & Timmermans, C., 2002. A compilation of high energy atmospheric muon data at sea level, *Astropart. Phys.,* **18,** 107–127.

Heck, D., Knapp, J., Capdevielle, J.N., Schatz, G. & Thouw, T., 1998. CORSIKA: A Monte Carlo code to simulate extensive air showers, Karlsruhe University, Forschungszentrum Karlsruhe Report FZKA 6019.

Jenneson, P.M., Gilboy, W.B., Simons, S.J.R., Stanley, S.J. & Rhodes, D., 2007. Imaging large vessels using cosmic-ray tomography muon energy-loss techniques. *Chem. Eng. J.,* **130,** 75–78.

Klimushin, S.I., Bugaev, E.V. & Sokalski, I.A., 2001. Parametrization of atmospheric muon angular flux underwater, *Phys. Rev. D,* **64,** 014016, doi:10.1103/PhysRevD.64.014016.

Komorowski, J.C., Legendre, Y., Caron, B. & Boudon, G., 2008. Reconstruction and analysis of sub-plinian tephra dispersal during the 1530 A.D. Soufrière (Guadeloupe) eruption: implications for scenario definition and hazards assessment, *J. Volcanol. Geoth. Res.,* **178,** 491–515.

Kudryavtsev, V.A., 2009. Muon simulation codes MUSIC and MUSUN for underground physics, *Compt. Phys. Commun.,* **180,** 339–346, doi:10.1016/j.cpc.2008.10.013.

Leprince-Ringuet, L., 1945. *Les rayons cosmiques. Les mésotons,* ed., Albin Michel, Paris.

Lesparre, N., Marteau, J., Déclais, Y. & Gibert, D., 2010. Design and operation of a field telescope for cosmic ray geophysical tomography, *Nucl. Instrum. Methods Phys. Res. A,* submitted.

Liu, Y., Derome, L. & Buénerd, M., 2003. Atmospheric muon and neutrino flux from 3-dimensional simulation, *Phys. Rev. D,* **67**(7), 073022(23 pages).

Malmqvist, L., Jönsson, G., Kristiansson, K. & Jacobsson, L., 1979. Theoretical studies of in-situ rock density determination using cosmic-ray muon intensity measurements with application in mining geophysics, *Geophysics,* **44,** 1549–1569.

Nagamine, K., 1995. Geo-tomographic observation of inner-structure of volcano with cosmic-ray muons, *J. Geography,* **104,** 998–1007.

Nagamine, K., 2003. *Introductory Muon Science*, Cambridge University Press, Cambridge, 208pp.

Nagamine, K., Iwasaki, M., Shimomura, K. & Ishida, K., 1995. Method of probing inner-structure of geophysical substance with the horizontal cosmic-ray muons and possible application to volcanic eruption prediction, *Nucl. Instrum. Methods A,* **356,** 585–595.

Neddermeyer, S.H. & Anderson, C.D., 1937. Note on the nature of cosmic-ray particles, *Phys. Rev.,* **51,** 884–886.

Neddermeyer, S.H. & Anderson, C.D., 1938. Cosmic-ray particles of intermediate mass, *Phys. Rev.,* **54,** 88–89.

Nicollin, F., Gibert, D., Beauducel, F., Boudon, G. & Komorowski, J.-C., 2006. Electrical tomography of La Soufrière of Guadeloupe Volcano: field experiments, 1D inversion and qualitative interpretation, *Earth planet. Sci. Lett.,* **244,** 709–724.

Pla-Dalmau, A., Bross, A.D. & Mellott, K.L., 2001. Low-cost extruded plastic scintillator, *Nucl. Instrum. Methods A,* **466,** 482–491.

Reyna, D., 2006. A Simple parameterization of the cosmic-ray muon momentum spectra at the surface as a function of zenith angle, preprint, arXiv:hep-ph/0604145.

Sanuki, T. *et al.*, 2002. Measurements of atmospheric muon spectra at mountain altitude, *Phys. Lett. B,* **541,** 234–242, doi: 10.1016/S0370-2693(02)02265-7.

Sokalski, I.A., Bugaev, E.V. & Klimushin, S.I., 2001. MUM: flexible precise Monte Carlo algorithm for muon propagation through thick layers of matter, *Phys. Rev. D,* **64,** 074015.

Stanley, S.J., Rhodes, D., Jenneson, P.M., Gilboy, W.B. & Simons, S.J.R., 2008. See inside: The development of a cosmic ray muon imaging system to aid the clean up of the UKs nuclear waste legacy. *Ann. Nucl. Energy,* **35,** 507–517.

Tanaka, H. & Yokoyama, I., 2008. Muon radiography and deformation analysis of the lava dome formed by the 1944 eruption of Usu,

Hokkaido—Contact between high-energy physics and volcano physics, *Proc. Japan Acad.,* **B84,** 107–116.

Tanaka, H., Nagamine, K., Kawamura, N., Nakamura, S.N., Ishida, K. & Shimomura, K., 2001. Development of the cosmic-ray muon detection system for probing internal-structure of a volcano, *Hyperfine Interact.,* **138,** 521–526.

Tanaka, H., Nagamine, K., Kawamura, N., Nakamura, S.N., Ishida, K. & Shimomura, K., 2003. Development of a two-fold segmented detection system for near horizontally cosmic-ray muons to probe the internal structure of a volcano, *Nucl. Instrum. Methods A,* **507,** 657–669.

Tanaka, H., Nagamine, K., Nakamura, S.N. & Ishida, K., 2005. Radiographic measurements of the internal structure of Mt. West Iwate with near horizontal cosmic ray muons and future developments, *Nucl. Instrum. Methods A,* **555,** 164–172.

Tanaka, H., Nakano, T., Takahashi, S., Yoshida, J., Ohshima, H., Maekawa, T., Watanabe, H. & Niwa, K., 2007a. Imaging the conduit size of the dome with cosmic ray muons: the structure beneath Showa Shinzan Lava Dome, Japan, *Geophys. Res. Lett.,* **34,** L22311, doi:10.1029/2007GL031389.

Tanaka, H. *et al.*, 2007b. High resolution imaging in the inhomogeneous crust with cosmic ray muon radiography: the density structure below the volcanic crater floor of Mt. Asama, Japan, *Earth planet. Sci. Lett.,* **263,** 104–113.

Tanaka, H., Nakano, T., Takahashi, S., Yoshida, J. & Niwa, K., 2007c. Development of an emulsion imaging system for cosmic-ray muon radiography to explore the internal structure of a volcano, Mt. Asama, *Nucl. Instrum. Methods A,* **575,** 489–497.

Tanaka, H. *et al.*, 2008. Radiographic imaging below a volcanic crater floor with cosmic-ray muons, *Am. J. Sci.,* **308,** 843–850.

Tanaka, H., Uchida, T., Tanaka, M., Shinohara, H. & Taira, H., 2009a. Cosmic-ray muon imaging of magma in a conduit: degassing process of Satsuma-Iwojima Volcano, Japan, *Geophys. Res. Lett.,* **36,** L01304, doi:10.1029/2008GL036451.

Tanaka, H. *et al.*, 2009b. Detecting a mass change inside a volcano by cosmic-ray muon radiography (muography): first results from measurements at Asama volcano, Japan, *Geophys. Res. Lett.,* **36,** L17302, doi:10.1029/2009GL039448.

Tang, A., Horton-Smith, G., Kudryavtsev, V.A. & Tonazzo, A., 2006. Muon simulations for Super-Kamiokande, KamLAND, and CHOOZ, *Phys. Rev. D,* **74,** 053007, doi:10.1103/PhysRevD.74.053007.

Tilav, S., Desiati, P., Kuwabara, T., Rocco, D., Rothmaier, F., Simmons, M. & Wissing, H., for the IceCube Collaboration, 2009. Atmospheric Variations as observed by IceCube, Proceedings of the 31st ICRC, Łódź.

Uchida, T., Tanaka, H. & Tanaka, M., 2009. Space saving and power efficient readout system for cosmic-ray muon radiography, *IEEE trans. Nucl. Sci.,* **56,** 448–452.

Volkova, L.V., Zatsepin, G.T. & Kuzmichev, L.A., 1979. *Sov. J. Nucl. Phys.,* **29,** 645–651.